Structure and Dynamics of Micelle-bound Human α-Synuclein*⑤

Tobias S. Ulmer‡§, Ad Bax‡, Nelson B. Cole¶, and Robert L. Nussbaum¶

From the ‡Laboratory of Chemical Physics, NIDDK and the ¶Genetic Disease Research Branch, National Human Genome Research Institute, National Institutes of Health, Bethesda, Maryland 20892

Misfolding of the protein α-synuclein (aS), which associates with presynaptic vesicles, has been implicated in the molecular chain of events leading to Parkinson's disease. Here, the structure and dynamics of micelle-bound aS are reported. Val³-Val³⁷ and Lys⁴⁵-Thr⁹² form curved α-helices, connected by a well ordered, extended linker in an unexpected anti-parallel arrangement, followed by another short extended region (Gly⁹³-Lys⁹⁷), overlapping the recently identified chaperone-mediated autophagy recognition motif and a highly mobile tail (Asp⁹⁸-Ala¹⁴⁰). Helix curvature is significantly less than predicted based on the native micelle shape, indicating a deformation of the micelle by aS. Structural and dynamic parameters show a reduced helical content for Ala³⁰-Val³⁷. A dynamic variation in interhelical distance on the microsecond timescale is complemented by enhanced sub-nanosecond timescale dynamics, particularly in the remarkably glycine-rich segments of the helices. These unusually rich dynamics may serve to mitigate the effect of aS binding on membrane fluidity. The well ordered conformation of the helix-helix connector indicates a defined interaction with lipidic surfaces, suggesting that, when bound to larger diameter synaptic vesicles, it can act as a switch between this structure and a previously proposed uninterrupted helix.

The protein α-synuclein (aS)[1] has been implicated in the molecular chain of events leading to Parkinson's disease, the second most common neurodegenerative disorder in humans (1–3). Lewy bodies and Lewy neurites found in Parkinson's disease in general contain aggregates of aS (4, 5), which is prone to form aggregates *in vitro* (6, 7). Moreover, three missense mutations (A30P, E46K, and A53T) in the gene encoding aS cause familial Parkinson's disease as well as aS gene trip-

lication (3, 8, 9). The amino acid sequence of aS consists of 140 residues with 7 copies of an unusual 11-residue repeat, followed by a hydrophilic tail (Fig. 1). Based on sequence analysis, it was suggested that aS interacts with lipid membranes through its repeat region (10, 11) and interactions with small unilamellar vesicles (SUVs) and micelles preferentially containing negatively charged head groups have been documented *in vitro* (10, 12–14). In accordance with those properties, aS localizes in a physiological environment at nerve termini in close proximity to synaptic vesicles (15, 16) and may be implicated in synaptic plasticity and neurotransmitter release (8, 9).

As evidenced by a number of biophysical techniques, aS is predominantly a random coil in aqueous solution but has been shown to adopt secondary structure of mostly helical nature upon association with negatively charged SUV or detergent micelle surfaces (10, 12, 13, 17). In every case, the repeat region mediates lipid or detergent interactions, whereas the hydrophilic tail remains free in solution. In the presence of SUV the large majority of aS molecules exist vesicle-bound (10). Based on the backbone ¹H-¹H NOE and secondary chemical shift pattern, helical secondary structure has been attributed to the entire repeat region in the micelle-bound state with the exception of a short stretch near Ser⁴²-Thr⁴⁴ (12, 18). When associated with SUVs of 300–400 Å diameter, electron paramagnetic resonance (EPR) data were interpreted as evidence for an uninterrupted helix extending throughout the entire repeat region (19). Helical wheel models have been proposed to describe the interaction of the helix side chains with the membrane surface (12, 18, 19). However, besides those qualitative properties no further structural information of the lipid-bound state of aS is available. The dynamic properties of aS along the helix and information on site-specific interactions of aS with lipidic surfaces are also unknown. Moreover, although aS adopts β-stranded conformation in the aggregated, fibrillar forms characteristic of Lewy bodies (20), aggregation of aS into dimers and multimers is promoted by lipid environments that induce an α-helical conformation (14, 21, 22). Thus, high resolution structural and dynamic information of aS in its helical conformation appears pertinent to developing a better understanding of the physiological role of aS, as well as possible structural features relevant to aS misfolding.

Here, the structure and dynamics of aS in the micelle-bound form, determined by solution NMR spectroscopy, are presented and related to the vesicle-bound state. As solution NMR is limited by particle size, the direct study of vesicle-bound aS is not feasible. We therefore elected to resort to smaller diameter micelles, which elicit a similar aS helical content as SUV (12).

EXPERIMENTAL PROCEDURES

Protein Production—The human α-synuclein (aS) gene was expressed from the kanamycin restricted, T7*lac* promoter controlled pET-41 vector (Novagen, Inc.). A mutant, aS(S87C), was constructed from this vector following the QuikChange protocol (Stratagene, Inc.). Both genes were overexpressed in *Escherichia coli* BL21(DE3) cells,

[1] The abbreviations used are: aS, human α-synuclein; EPR, electron paramagnetic resonance; PRE, paramagnetic relaxation enhancement; RDC, residual dipolar coupling; SUV, small unilamellar vesicle; TROSY, transverse relaxation optimized spectroscopy; NOE, nuclear Overhauser effect; NOESY, NOE spectroscopy; TOCSY, total correlation spectroscopy; TEMED, *N,N,N',N'*-tetramethylethylenediamine; HSQC, heteronuclear single quantum coherence; CT, constant time.

cultured in M9 minimal medium (6 g/liter $Na_2HPO_4 \cdot 7H_2O$, 3 g/liter KH_2PO_4, 0.5 g/liter NaCl, 1 mM $MgSO_4$, 100 μM $CaCl_2 \cdot 2H_2O$, and D-glucose/NH_4Cl as specified below). 1 g/liter 98% $^{15}NH_4Cl$ was employed to achieve ^{15}N enrichment. 2 g/liter 99% [^{13}C]glucose, 1 g/liter 98% $^{15}ND_4Cl$, and 1 g/liter 98% D/99% ^{13}C/98% ^{15}N-rich growth medium supplement (Isogro, Isotec, Inc.) in D_2O solution were employed to label with ^2H/^{13}C/^{15}N. Uniformly ^2H/^{13}C/^{15}N-enriched protein with selectively protonated Val-$\gamma^{1,2}$, Leu-$\delta^{1,2}$, and Ile-δ^1 methyl groups was prepared by using 2 g/liter 97% D, 99% [^{13}C]glucose, 1 g/liter 98% $^{15}ND_4Cl$ in D_2O solution, and, added 45 min before protein induction, 50 mg/liter 3,3-$^2H_2$-, α-[^{13}C]ketobutyrate, and 100 mg/liter 3-^2H-, α-[^{13}C]ketoisovalerate (23). Protein expression was induced at A_{600} = 0.8 for 2 h in H_2O or 4 h in D_2O. Purification involved heat precipitation (10 min, 80 °C) of the cells in 50 mM Tris·HCl, pH 7.5, 500 mM NaCl (2 mM β-mercaptoethanol for S87C). Subsequent ion-exchange chromatography on Q-Sepharose (Amersham Biosciences) yielded >98% pure protein of the correct mass as judged by SDS-PAGE and electrospray mass spectrometry.

NMR Sample Preparation—All samples were prepared in H_2O to contain aS at a concentration of 0.5 mM (ϵ_{280} = 5120 $M^{-1}cm^{-1}$), 75 mM SDS, 6% D_2O, and 0.02% (w/v) NaN_3 in a total volume of 270 μl. Nine samples were prepared. Sample A was enriched only in ^{15}N, sample B was uniformly enriched in ^2H/^{13}C/^{15}N, sample C in ^2H/^{13}C/^{15}N, but selectively protonated at Val-$\gamma^{1,2}$, Leu-$\delta^{1,2}$, and Ile-δ^1 methyl groups and also employed deuterated SDS. Samples D and E used ^2H/^{13}C/^{15}N-enriched aS in the presence of charged stretched polyacrylamide gels (see below). Samples F–H employed ^2H/^{13}C/^{15}N-enriched aS(S87C) tagged with cysteaminyl-EDTA, complexed with Ca^{2+}, Mn^{2+}, and Co^{2+}, respectively. Samples A–E were buffered by 20 mM NaH_2PO_4/Na_2HPO_4, pH 7.4, and samples F–H by 20 mM HEPES·NaOH, pH 7.4. The last sample, I, contained ^2H/^{13}C/^{15}N-labeled aS, buffered by 20 mM Tris·HCl, pH 8.4.

The gel for sample D was polymerized from a 4.6% w/v solution of acrylamide (AA), 2-acrylamido-2-methyl-1-propanesulfonate (AMPS), and bisacrylamide with a monomer to cross-linker ratio of 39:1 (w/w) and a molar ratio of 96:4 of AA to AMPS. To allow easy comparison between gels containing different amounts of charged monomer, AMPS is counted here as AA and the AMPS:AA ratio is specified separately. Gel for sample E was polymerized from a 5.2% w/v solution of AA, AMPS, and piperazine diacrylamide as cross-linker with a monomer to cross-linker ratio of 39:1 (w/w) and a molar ratio of 98:2 of AA to AMPS. For the reported monomer to cross-linker ratio, piperazine diacrylamide was counted as bisacrylamide to again allow for direct comparison between gels. Polymerization was initiated by the addition of ammonium persulfate and TEMED at 0.1% w/v and v/v, respectively, and allowed to proceed in a cylinder of 5.4-mm diameter for 3 h at 23 °C. Subsequently, gels were dialyzed, dried, soaked with protein solution for 2 days, and transferred to NMR tubes as described (24, 25). ^2H quadrupolar splittings of 1.2 and 1.7 Hz were measured for samples D and E, respectively.

A 20 mM HEPES·NaOH, pH 8.0, 200 mM NaCl, 25 mM EDTA, 0.02% NaN_3 solution of 50 μM aS(S87C) containing 1 mM dithiothreitol was exchanged into the dithiothreitol-free solution containing 1 mM *N*-[*S*-(2-pyridylthio)cysteaminyl]-EDTA (Toronto Research Chemicals, Inc.) by ultrafiltration and allowed to react overnight at room temperature. Small amounts of homodimeric aS(S87C) were removed by ion-exchange chromatography, and aS(S87C)-cysteaminyl-EDTA was exchanged into 20 mM HEPES·NaOH, pH 7.4, 50 mM NaCl by ultrafiltration. The EDTA tag was then charged by adding a 1.2 times excess of the desired ion over the protein, washed extensively with 20 mM HEPES·NaOH, pH 7.4, 700 mM NaCl to remove non-specifically bound ions, and exchanged into 20 mM HEPES·NaOH, pH 7.4, 0.02% NaN_3 by ultrafiltration. Samples were completed by the addition of SDS and D_2O to 75 mM and 6%, respectively.

NMR Spectroscopy—All experiments were carried out at 25 °C on Bruker spectrometers operating at ^1H frequencies of 600, 750, and 800 MHz equipped with cryogenic (600 MHz) or room temperature (750 and 800 MHz) probes. Data were processed and analyzed with the nmrPipe package (26). Throughout most experiments, the TROSY N-H component was selected (27, 28). H^N, N, C^α, and C′ assignments were made from HNCA, HN(CO)CA, HNCO, and HN(CA)CO experiments using sample B and the reported H^N, N, and C^α assignments (12). Subsequently, H^α and partial H^β assignments were obtained from TOCSY-TROSY experiments (sample A, τ_{mix} = 36 ms). CH_3 assignments of Val-$\gamma^{1,2}$, Leu-$\delta^{1,2}$, and Ile-δ^1 moieties of sample C were based on (H)CCONH and H(C)CONH experiments (29).

H^N-H^N NOEs were measured from HSQC-NOESY-TROSY experiments (sample B, τ_{mix} = 170 ms), H^N-H^α NOEs from NOESY-TROSY

experiments (sample A, τ_{mix} = 100 ms), H^N-$H^{\gamma,\delta\ (Val/Leu/Ile)}$ NOEs from NOESY-TROSY experiments (sample C, τ_{mix} = 150 ms), and CH_3-CH_3 NOEs from CT-HSQC-NOESY-CT-HSQC experiments (sample C, τ_{mix} = 150 ms).

$^3J_{C'C\gamma}$ and $^3J_{NC\gamma}$ couplings for aromatic and aliphatic residues were obtained from quantitative *J*-correlation spectroscopy (30, 31) with dephasing times of 60 and 160 ms, respectively. $^1J_{NH}$, $^1J_{C\alpha C'}$, and $^1J_{C'N}$, and $^1J_{NH} + ^1D_{NH}$, $^1J_{C\alpha C'} + ^1D_{C\alpha C'}$, $^1J_{C'N} + ^1D_{C'N}$ couplings were determined from mixed-constant time, H^N-coupled HNCO, C^α-coupled HNCO, or quantitative *J*-correlation HN(CA)CO (32) and quantitative *J*-correlation HNCO experiments (33) of samples B, D, and E, respectively.

The ^{15}N relaxation parameters R_1, R_2, and {^1H}-^{15}N NOE were determined at 60.8-MHz for sample B (34, 35). For the {^1H}-^{15}N NOE measurement, 5 s of presaturation preceded by a recycling delay of 4 s were used for the NOE experiment and a 9-s recycle delay for the reference experiment. Mn^{2+}-induced paramagnetic relaxation enhancements (PRE) of $^1H^N$ transverse magnetizations, Γ_2, were determined from the difference in $R_2(^1H^N)$ of the Ca^{2+}- and Mn^{2+}-loaded samples, employing the pulse sequence described in Ref. 36. Co^{2+}-induced pseudo-contact shifts were found to result in peak doubling of resonances close to the metal ion, indicating the presence of two diastereomers for the cysteaminyl·EDTA·Co^{2+} complex and, for this reason, were not pursued further.

Structure Calculation—Due to the pronounced differences in dynamics experienced by the RDC (see "Results"), the local geometry of Val[3]-Lys[97], exhibiting general order parameters (S^2) above 0.5, was generated by molecular fragment replacement (37). The remaining residues are represented by random-coil conformations. A fragment length of 7 residues, 372 H^α, N, C^α, and C′ chemical shifts, and 520 $^1D_{NH}$, $^1D_{C\alpha C'}$, and $^1D_{C'N}$ residual dipolar couplings (RDCs) were used for molecular fragment replacement, allowing the alignment tensor for each fragment to be an adjustable parameter. For each fragment ten candidates in best agreement with the chemical shifts and RDCs were selected from the molecular fragment replacement data base (37). Backbone dihedral angles were then determined by averaging over all selected candidates of all (overlapping) fragments containing any given angle, but excluding fragments where this angle is located in its N- or C-terminal residue. The alignment tensor magnitudes, D_a, calculated for this average structure varies little with fragment lengths ranging from 7 to 11 residues (Supplementary Fig. 1), indicating that dynamics is not significantly impacting the fragment structures over this length range. Standard deviations for the angles were typically between 2 and 10° for most residues, and between 10 and 25° for Ala[30]-Thr[44]. The local geometry thus defined was implemented as backbone dihedral restraints in subsequent structure calculations with the program Xplor-NIH 2.9.5 (38).

The backbone H^N-$H^{N,\alpha}$ NOEs were found to be in good agreement with this generated structure, and side-chain conformations were restricted by H^N-$H^{\gamma(Ile/Thr)}$, H^N-$H^{\delta(Val/Leu)}$ and CH_3-CH_3 NOEs. For residues with non-rotamer-averaged $^3J_{C'C\gamma}$ and $^3J_{NC\gamma}$ couplings, the χ_1 rotamer state was selected based on those couplings (30, 31). For the translation of PRE Γ_2 values into distances, the cysteaminyl-EDTA-Mn^{2+} group was represented by an ensemble of three structures during simulated annealing, and the model-free Solomon-Bloembergen equations were applied (39). The Γ_2 values of repeat region residues exhibited a constant, reproducible background (Supplementary Fig. 2), which was subtracted (6 Hz) to achieve agreement between the position of the paramagnetic tag and helix-C, *i.e.* internal referencing was performed. For helix-N the H^N intensity ratios between dia- and paramagnetic samples, $I_{Mn}{}^{2+}/I_{Ca}{}^{2+}$, followed the Γ_2 values except for the first nine residues (Supplementary Fig. 2), suggesting some variation in distance between helix-N and -C with more distant conformers contributing overproportionally to the ensemble-averaged $R_2(Mn^{2+})$ rate, *i.e.* the calculated interhelical distances will be somewhat biased to more remote distances than the actual average. In order not to introduce opposing restraints, the structure was calculated by only considering the Γ_2 values of Lys[10]-Lys[21] of helix-N, besides the values for helix-C. It is also noted that the paramagnetic tag is clearly oriented to one side of helix-C (Supplementary Fig. 3). To aid in the placement of the helices relative to each other, global alignment tensors were used to describe RDC for residues with S^2 > 0.8 and with fragment number exhibiting $|D_a|$ > 6 Hz (residues 9–23, 54–63, and 70–81 for sample D and residues 9–23, 57–63, and 70–81 for sample E).

Simulated annealing calculations were carried out from 500 to 0 K in the presence of an empirical backbone-backbone hydrogen-bonding potential (40) and torsion angle potentials of mean force (41). In order not to distort helix-C by the relatively strong forces acting on the paramagnetic tag, the dihedral angle restraints of residues 85–88 were tightened. To allow a wider range of helix-helix orientations, the dihedral

FIG. 1. **Amino acid sequence of human α-synuclein (aS).** The seven imperfect 11-residue repeats are labeled in *Roman numerals* with their second to sixth residues (predominantly KTKEGV) highlighted in *red*. Ser[9]-Ala[89] are referred to as the "repeat region" and Asp[98]-Ala[140] as the "tail region" of aS. Residues found to be in helical conformation in micelle-bound aS are *underlined*.
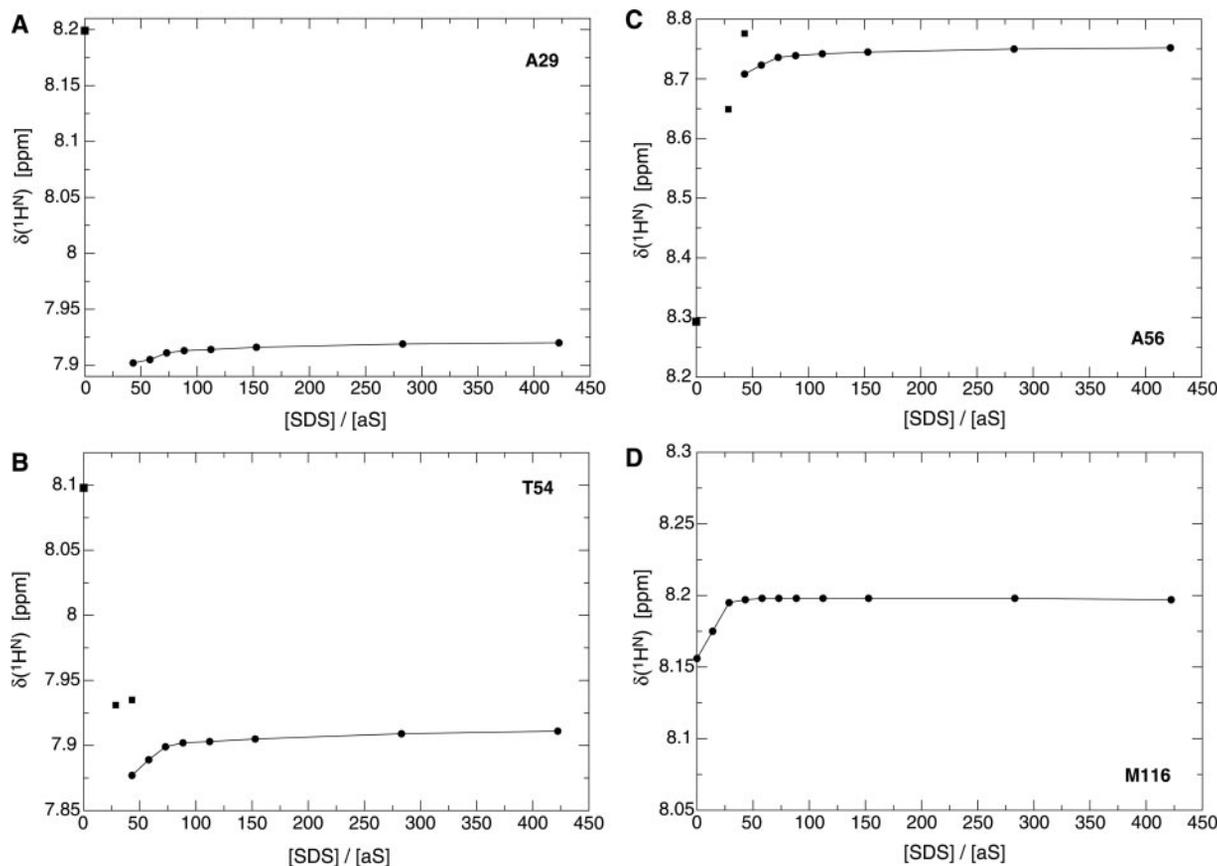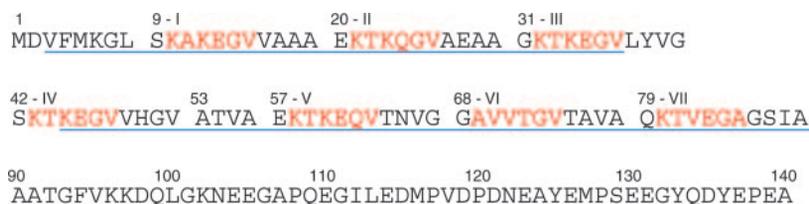
FIG. 2. **Titration of aS with SDS.** The amide proton ($^1H^N$) chemical shifts of Ala[29] (*A*), Thr[54] (*B*), Ala[56] (*C*), and Met[116] (*D*) are shown as a function of molar SDS:aS ratio. Fast exchange kinetics were observed for SDS:aS ≥ 58:1, and data points are represented by *circles*; below this ratio complex exchange behavior was observed and data points are shown as *squares*. For several residues (*e.g.* Thr[54] and Ala[56]) a doubling of resonances is observed at an intermediate SDS:aS ratio of 43:1. For Ala[29] and Thr[54], the chemical shift in the absence of SDS is far off the curve toward the final micelle-bound state. At low SDS:aS ratios extensive resonance broadening prevented the identification of chemical shifts for residues of the aS repeat region (Fig. 1).

angle restraints of residues 39–43 were relaxed. The energy-minimized average structure, calculated from the ensemble of 20 lowest energy structures, was deposited in the protein data base under accession code 1XQ8.

SDS Titration—Titrations were performed in 20 mM NaH$_2$PO$_4$/Na$_2$HPO$_4$ (pH 7.4)/6% D$_2$O at 25 °C and 800 MHz. The aS starting concentration was 0.2 mM, and 11 titrations steps were performed from aS:SDS molar ratios of 0:422 (Fig. 2). At each titration point a TROSY-HSQC spectrum was recorded ($t_{15N,max}$ = 144.9 ms, $t_{1HN,max}$ = 113.9 ms). In the absence of SDS selected aS assignments were made based on an HNCA experiment and comparison of aS wild-type spectra with spectra of aS mutants A30P and A53T. Between aS:SDS ratios of 14 to 43 the assignment of a few residues with characteristic chemical shift was made. For aS:SDS ratios ranging from 58 to 422 peaks shift relatively little and assignments followed directly from the assignments of sample B (*cf.* above).

RESULTS

Association of aS with SDS Micelles Is Quantitative and Not Strongly Dependent on the Chemical Makeup of the Micelle— The transition of aS from the free to the micelle-bound state has been examined by NMR spectroscopy to monitor the structuring of aS and to assess the tightness of aS binding to a

micelle composed of SDS molecules. A tight interaction is mandatory for structure determination by NMR. Subsequently, mixed-micelles in which 70% of the SDS molecules have been replaced by the lipid-like detergent dodecyl phosphocholine (DPC) were compared with SDS-only micelles to assess the influence of micelle chemical makeup on aS structural properties. In the presence of aS, a SDS micelle was estimated to contain ∼70 SDS molecules (12). Consequently, up to a molar aS:SDS ratio of ∼1:70, multiple aS molecules may bind to a single micelle. A titration with SDS was carried out to cover molar aS:SDS ratios ranging from 0 to 422 at an initial aS concentration of 0.2 mM. Chemical shift changes of the backbone $^1H^N$ and ^{15}N nuclei of each residue were monitored during the titration, and the $^1H^N$ chemical shift changes of four residues, Ala[29], Thr[54], Ala[56], and Met[116], are presented here (see Fig. 2). Changes in chemical shifts are sensitive indicators of changes in local structure and, thus, excellent probes of the transition of aS from the free to the micelle-bound state.

The first titration step, to an aS:SDS ratio of 1:14, broadened the resonances of the entire repeat region of aS (Fig. 1) essen-

tially beyond detection. The broadening may arise from the binding of multiple copies of aS, resulting in large particle sizes, or exchange kinetics that is intermediate on the NMR timescale. As the titration progresses (aS:SDS = 1:29), the missing resonances reappear at new positions. For residues of the C-terminal tail region (Fig. 1), no significant change in signal intensity was observed during these two titration steps, but essentially all of their very small shift changes take place there (Fig. 2*D*). At an aS:SDS ratio of 1:43, two species arise for each repeat region residue, one resonance that often, but not always, appears close to the previous titration step and one that is headed toward the final micelle-bound state (Fig. 2*C*). At aS:SDS ratios of 1:58 and higher only one resonance was observed for all residues, which asymptotically approached the final micelle-saturated state (Fig. 2, *A–C*). In good agreement with the previous estimate of the SDS micelle size (12), the chemical shift changes for repeat region residues leveled off rapidly after the titration point at an aS:SDS ratio of 1:73 was reached (Fig. 2, *A–C*), *i.e.* after each micelle had at most a single aS molecule bound, showing that quantitative aS·micelle complex formation had occurred.

Remarkably, for most residues of the repeat region, if not all, the chemical shift in the absence of SDS does not fall on the smooth curve toward the final micelle-saturated state (Fig. 2, *A* and *B*), indicating that the repeat region progresses through an intermediate state to reach the micelle-saturated state. Given the excess of aS over micelles, this intermediate state could involve two or more micelle-bound aS molecules. However, an analogous titration monitored by circular dichroism spectroscopy has found the aS helical content to increase until a aS:SDS ratio of ~1:70 is reached (12), indicating that below this ratio the free aS state remains populated and/or that, within such higher order complexes, aS is structurally different from its final helical, micelle-bound state.

When comparing the aS backbone H^N and N chemical shifts in the presence of an excess of SDS-only micelles and mixed micelles composed of DPC and SDS at a molar ratio of 70:30, most shifts agreed to within ±0.1 and ±1.0 ppm for H^N and N nuclei, respectively (Fig. 3 and Supplementary Fig. 4). The magnitude of these shift changes was relatively small, suggesting that the chemical makeup of SDS micelles does not strongly affect the aS structure. The most significant deviations were observed for residues located before and after the aS repeat region (Fig. 1) as well as those near the reported interruption of helical structure around Ser^{42}-Thr^{44} (12, 18). Minor structural rearrangements of these regions are a likely consequence of a change in micelle shape or diameter, or a subtle change in the interaction with the micelle itself. In conclusion, the chemical makeup of SDS micelles did not strongly affect the aS structure, and, when there was an excess of SDS micelles over aS molecules, quantitative binding occurred, allowing the structure determination of micelle-bound aS.

Micelle-bound aS Arranges into Two Curved, Anti-parallel Helices—The structure of micelle-bound aS was determined by solution NMR spectroscopy, relying on residual dipolar couplings (RDCs), measured in negatively charged stretched polyacrylamide gels (24, 42), in conjunction with long range distance information from Mn^{2+}-induced paramagnetic relaxation enhancements (PREs) (39, 43). The presence of the gel matrix did not influence the backbone chemical shifts (H^N, N, $C^α$, and C′) and, hence, the structure of micelle-bound aS (data not shown). To introduce the Mn^{2+} ion at a defined site of aS, an EDTA-derived tag was introduced to S87C-substituted aS, which is otherwise devoid of Cys residues. Chemical shift changes ensuing from the S87C substitution and the presence of the tag were restricted to the immediate vicinity of residue
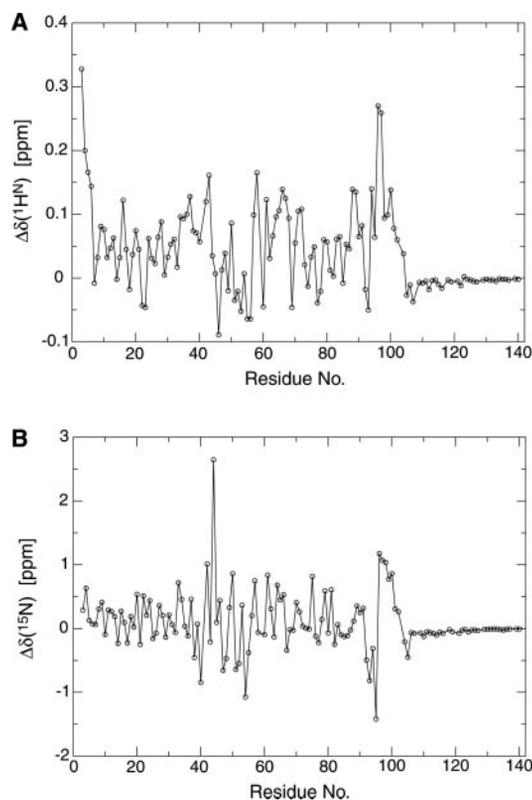
FIG. 3. **Effect of detergent on aS chemical shifts.** *A* and *B*, $^1H^N$ and ^{15}N chemical shift changes of aS when associated with SDS-only micelles and mixed micelles, composed of dodecyl phosphocholine (DPC) and SDS present at a molar ratio of 70:30. The chemical shifts were recorded at 25 °C and 750 MHz in 20 mM NaH_2PO_4/Na_2HPO_4, pH 7.4. Assignments for the mixed micelle state were transferred from the SDS-only state through a titration with DPC, as exemplified in Supplementary Fig. 4.

87 (Supplementary Fig. 5), showing that the aS structure is not unduly perturbed by the tagging.

The structure of micelle-bound aS consists of two curved α-helices, termed helix-N (Val^3-Val^{37}) and helix-C (Lys^{45}-Thr^{92}), connected by a short linker in an anti-parallel arrangement, followed by a short extended region (Gly^{93}-Lys^{97}) and a predominantly unstructured mobile tail (Asp^{98}-Ala^{140}; Fig. 4). Thus, helix-N essentially starts with the beginning of the aS sequence, before the first imperfect repeat, and ends in the third repeat (Fig. 1). The linker then takes up 7 residues before helix-C commences in repeat IV and extends throughout the remainder of the repeat region and terminates after three further residues (Fig. 1). The helix-helix connector forms an extended conformation with a turn propensity near its midpoint (Fig. 4*D*). Although it has been known that there is a discontinuity in the helical conformation of micelle-bound aS near Ser^{42}-Thr^{44} (12, 18), the anti-parallel orientation of the helices before and after this break was unexpected. Some variability in interhelical distances was evident from the PRE data, and the structure calculated is somewhat biased to more remote interhelical distances than the actual average (see "Experimental Procedures"). At a range of interhelical distances, including the calculated one, the side chains emanating from the helices were too far apart to interact with each other across the helices (Fig. 4*C*). An average of 3.60 ± 0.13 residues make up one turn of helix-N with an average twist angle of 100.1 ± 3.8°; for helix-C these parameters are 3.56 ± 0.16 and 101.2 ± 4.7°. Those parameters are not very sensitive to deviations from linear α-helical geometry (44). The diameter of a circle best-fitted to the helix and the bending angle between successive local helix axes calculated for 4 residue stretches are better
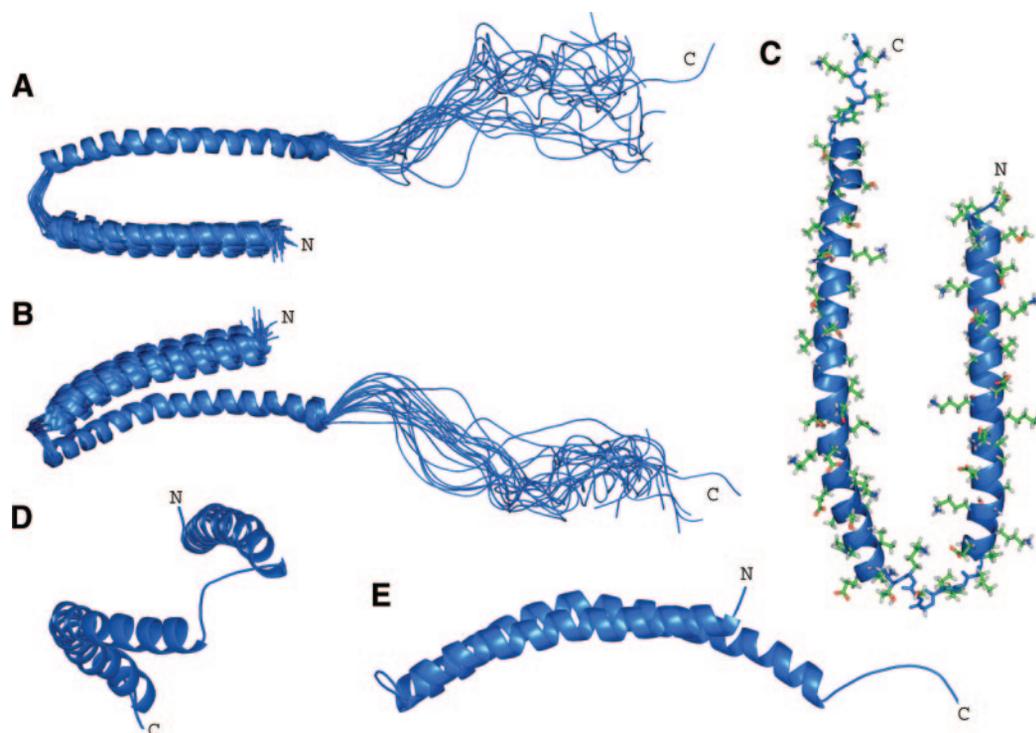
FIG. 4. **Structure of micelle-bound aS.** *A* and *B*, ensemble of twenty structures superimposed on helix-C. Helix-N (Val[3]-Val[37]) and helix-C (Lys[45]-Thr[92]) are connected by a short linker, followed by another short extended region (Gly[93]-Lys[97]) and a predominantly unstructured tail (Asp[98]-Ala[140]). The backbone root mean square deviation of the average aS structure for Val[3]-Lys[97] of the ensemble is 1.0 Å and does not reflect the much larger fluctuations present in this structure (*cf.* text). In particular, Ala[30]-Val[37] experience large amplitude dynamics and the depicted structure is merely a representation of the effective average conformation of the molecule. Views *A* and *B* are related by a rotation of ∼120° around the *x*-axis. Helix definitions are from Ref. 66. *C–E*, average structure. The helices appear to twine themselves around the micelle; the predominantly unstructured tail has been omitted. The depicted orientations are interconvertible by rotations of ∼90°.

indicators of helix curvature (44, 45). For helix-N the average circle diameter and bending angle were 153 Å and 10.1 ± 5.2°, respectively, whereas for helix-C values of 82 Å and 10.7 ± 6.8°, respectively, were obtained. A slight kink near Val[66]-Gly[67]-Gly[68], which "incorporates" curvature, appears partly responsible for the stronger bending of helix-C and allows the other stretches of helix-C to wrap around the micelle more intimately (Fig. 4, *C–E*).

Backbone Dynamics Vary Distinctly within the Helical Regions of Micelle-bound aS—The above-mentioned variation in interhelical distances suggests that dynamic processes play an important role in the understanding of aS structure, and, therefore, backbone dynamics were explored quantitatively. On a fast timescale (picoseconds to nanoseconds), ^{15}N relaxation measurements furnish the general order parameter, S^2 (46), which ranges from 0 to 1. Largely unstructured regions, such as the aS tail, adopt low S^2 values and structured regions, such as the repeat region, yield high S^2 values (Fig. 5A). On an intermediate timescale (nanoseconds to milliseconds), relative variations in the RDC-derived local alignment tensor magnitudes, D_a, report spatial fluctuations of the protein backbone (47, 48). A difference in D_a between two regions implies enhanced dynamics for the region with lower absolute value of D_a relative to the one with higher D_a (Fig. 5C). Finally, motions taking place on a slow timescale (milliseconds to seconds) have been studied by examining amide proton exchange with the solvent, expressed as the ratio of H-N signal intensities obtained with and without selective solvent inversion, I/I_0, at pH 8.4 (Fig. 5B).

A significant degree of correlation was obtained between S^2 and I/I_0 (Fig. 5, *A* and *B*). Residues with high S^2 values are also protected from solvent exchange, *i.e.* maintain hydrogen bonds for a larger fraction of time. There are three distinct regions within the repeat region that exhibit relatively low S^2 values,

Ala[30]-Val[37], Asn[65]-Val[70], and Glu[83]-Ala[89], and these regions also show the highest solvent exchange rates, except for Ser[42]-Lys[43]. The absence of hydrogen bonds for these latter two residues of the helix-helix connector agreed with its mostly extended conformation (Fig. 4D), for which no intramolecular hydrogen bonds could be formed. It is also noted that the helix-helix connector was well ordered on the sub-nanosecond timescale (Fig. 5A). On the intermediate timescale (Fig. 5C), the situation was somewhat different (Fig. 5C). Ala[30]-Val[37] and the helix-helix connector exhibited considerable dynamics, but also the beginning of helix-C (Lys[45]-Ala[56]) showed large amplitude motions. The striking difference with the dynamic events on the two other timescales suggests that the RDC-derived dynamics is dominated here by processes between those two timescales, *i.e.* on the microsecond timescale.

What structural fluctuations correspond to the dynamic events experienced by aS? To obtain parameters that describe the structure adopted by aS, the chemical shift changes of the backbone H^N, N, and C^α nuclei between the free and micelle-bound states of aS were computed. Each nucleus has different susceptibilities to structural parameters. C^α chemical shifts depend largely on the structural environment (average backbone dihedral angles), whereas H^N and N shifts do so to a much lesser extent and are also strongly influenced by the chemical environment, side-chain conformation and, in the case of H^N nuclei, hydrogen bonding (49, 50). The dynamics on the fast (nanosecond to picosecond) and slow (millisecond to second) timescales correlated well with the deviation of the C^α shifts from their random-coil positions (Fig. 6A). The correlation with the H^N shift changes are similar, indicating hydrogen bond formation, whereas for N no clear correlation was discernible (Supplementary Fig. 6). It appears that, for the two helices, the dynamic events on the fast and slow timescales reflect the local helical content. For example, the time fraction over which
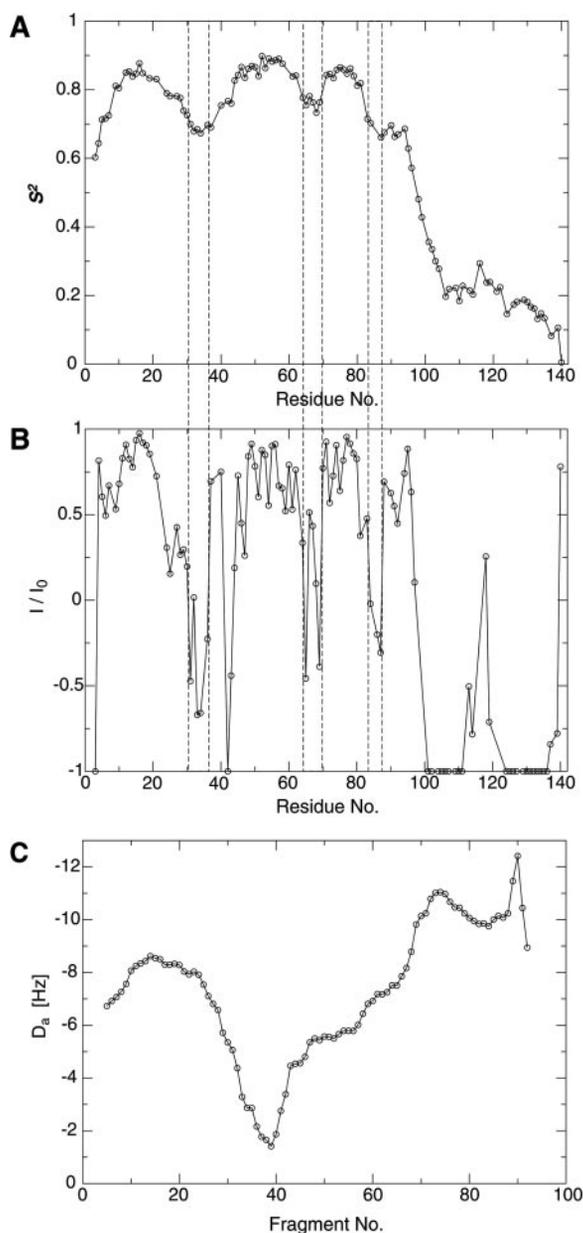
FIG. 5. **Backbone dynamics of micelle-bound aS.** *A*, general order parameter, S^2, derived from backbone ^{15}N relaxation analysis using an isotropic model (67). An isotropic correlation time of 15.1 ns was obtained. *B*, exchange of the backbone amide protons (H^N) with the solvent; depicted as the ratio of H-N TROSY signal intensities obtained with and without selective solvent inversion, I/I_0, at pH 8.4. The solvent was inverted 50 ms prior to the start of the pulse sequence, and radiation damping was suppressed by the application of weak gradient pulses during this period (68). ^{15}N Boltzmann magnetization was eliminated, and during the pulse sequence and recycle delay the solvent was placed at $+I_z$ whenever possible. Resonances that were absent in the pH 8.4 spectrum compared with pH 7.4 spectrum were assigned I/I_0 values of -1. An $I/I_0 = 0$ ratio corresponds to a H^N exchange rate of $\sim 14 \text{ s}^{-1}$. *C*, variation of the alignment tensor magnitude, D_a, obtained during molecular fragment replacement using a fragment length of 7 residues, along the sequence. The *fragment number* denotes the center residue of each fragment. No unique local structure could be found for fragments involving the highly mobile tail residues, and therefore no D_a values are available for this region.

residues Ala^{30}-Val^{37} are α-helical is considerably diminished as judged by the $\sim 50\%$ smaller C^α secondary shifts and the enhanced slow and fast timescale dynamics compared with the other helical regions. It is therefore not surprising that the magnitude of the RDCs of this region, *i.e.* of the alignment, is greatly diminished relative to its preceding helical region, or
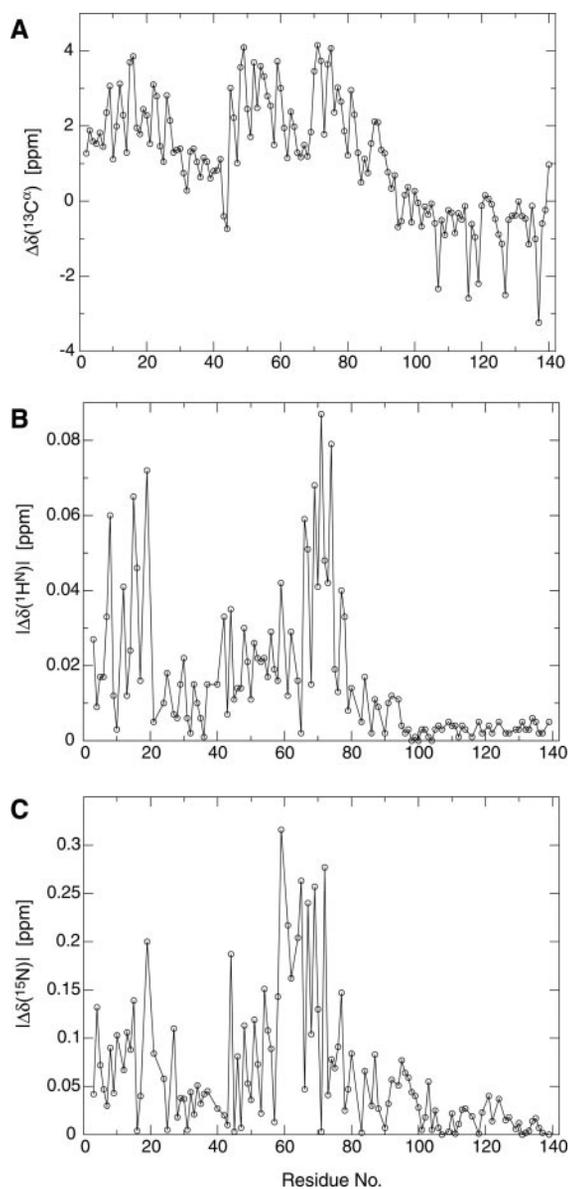
FIG. 6. **Chemical shift changes of aS upon micelle binding.** *A*, difference of observed C^α chemical shift and random coil values as a function of residue number. $^{13}C^\alpha$ secondary shifts are reported relative to the random coil values of Ref. 69 but have not been corrected for the $\sim +0.5$-ppm isotope shift resulting from perdeuteration of the carbon-attached hydrogens. The shift changes correlate with S^2 and I/I_0 (Fig. 5, *A* and *B*). *B* and *C*, absolute $^1H^N$ and ^{15}N chemical shift changes of aS between molar SDS:aS ratios of 58:1 and 422:1. These shift changes reflect aS structural changes between the intermediate state(s) present during the SDS titration and the micelle-saturated state. A qualitative correlation with the variation in D_a (Fig. 5*C*) is observed: Lys^{60}-Thr^{75} show the largest H^N and N shift changes, followed by Met^5-Glu^{20} for H^N shifts, then by Ser^{42}-Val^{55} and finally by Ala^{30}-Val^{40}.

helix-C within Glu^{83}-Ala^{89}. A static structure for this stretch of helix-N does not reflect the actual dynamic events taking place, but merely describes the effective average conformation of the molecule. However, the elevated dynamics on the microsecond timescale observed for the Lys^{45}-Ala^{56} region was somewhat surprising given its high S^2 values and large C^α secondary shifts, which were comparable to regions with low microsecond timescale dynamics. It follows that, for this region, helical conformation must be maintained throughout any dynamic events taking place. Rather than helix fraying, which will contribute to the large amplitude angular fluctuations of Ala^{30}-Val^{37}, motions in Lys^{45}-Ala^{56} must involve larger units of well structured helix, *i.e.* global rather than local motions.

The presence of motions between secondary structure elements (global motions) for the aS·micelle system agreed well with the PRE data, and it follows that the detected variation in interhelical distances takes place predominantly on the microsecond timescale. It is also noted that the continuous association and/or dissociation of the aS·micelle complex likely take place on this timescale. The variation in D_a did not correlate with the chemical shift changes between the free and micelle-bound states (Figs. 5*C*, 6*A*, and Supplementary Fig. 6), but weakly with the shift changes between the intermediate state(s) present during the SDS titration and the micelle-saturated state (Figs. 5*C*, 6*B*, and 6*C*). Unfortunately, the structural changes reflected by these chemical shift changes are unknown.

Structural Basis for the Binding of the Negatively Charged Micelle Surface—To illustrate the interaction of aS with the micelle surface and to examine possible site-specific differences, the electrostatic surface potential of micelle-bound aS has been evaluated (Fig. 7). The inner surface of the curved helices is largely apolar. Most of the basic side chains point sideward from the helices, and the acidic side chains predominantly line their outer surface. To interact with the micelle surface the inner surface of the helices is prone to move past the charged headgroups and interact with the apolar detergent or lipid tails. Concomitantly, the sideward oriented positively charged side chains can engage in interactions with the negatively charged headgroups and thus explain the preference of aS-vesicle interactions on the presence of lipids with negatively charged headgroups (10). Effectively, aS absorbs on the micelle surface and alters its surface charge density, a mode of interaction that classifies it as a hydrophobic cation (51). The helix-helix connector exhibited, with Leu[38], Tyr[39], Val[40], Lys[43], and bordering Lys[45], a particularly pronounced hydrophobic cationic character (Fig. 7*B*), which, in turn, may explain its relatively high degree of backbone order on the sub-nanosecond timescale (Fig. 5*A*).

The diameter of a free micelle composed of ~70 SDS molecules is expected to be ~46 Å (52). However, helix-C appeared to encompass a particle with a much larger diameter of 82 Å (Fig. 4, *D* and *E*), indicating the desire to form a less curved helix than a globular SDS micelle would support. Is the native, globular micelle shape deformed by the interaction with aS or do the pronounced microsecond timescale dynamics at the end and beginning of helix-N and -C, respectively, indicate their only transient interaction with the micelle surface? In the presence of hydrophobic cations it has been shown that anionic SDS micelles undergo uniaxial growth from globular micelles to prolate ellipsoidal structures due to a decrease of the electrostatic repulsion of headgroups (53). Thus, it appears that a deformation of the globular micelle along the helix axes to an ellipsoid particle can account for the observed diameter of helix-C. In addition to a deformation of the micelle shape, slight differences in the immersion depth of individual helix regions can also contribute to the observed helix diameter. For Ala[30]-Val[37] of helix-N the helical content is greatly diminished as judged by the very small secondary $^{13}C^\alpha$ shifts (Fig. 6*A*), the rapid backbone amide exchange rates (Fig. 5*B*), and the high degree of sub-nanosecond timescale dynamics (Fig. 5*A*) compared with the other helical regions of aS. These characteristics of Ala[30]-Val[37] may contribute to the larger apparent diameter of curvature for helix-N (153 Å) compared with helix-C, in addition to its shorter length than helix-C.

Finally, given that the helices N and C are at variable, relatively close distances and the charges of the basic side chains are shielded by the negatively charged SDS headgroups, an attempt was made to locate short range interproton dis-
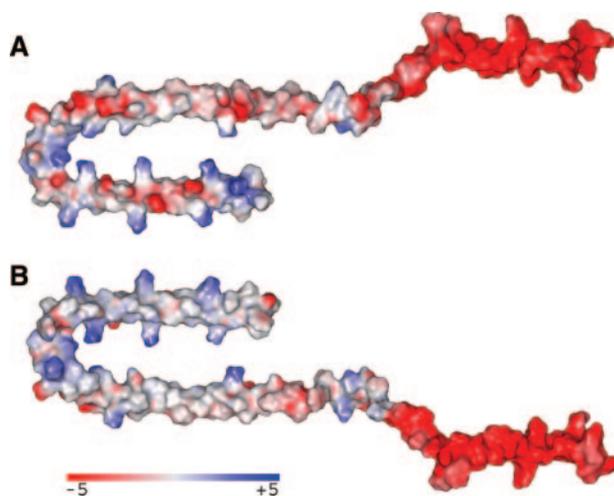
FIG. 7. **Charge distribution of micelle-bound aS.** *A* and *B*, *top* and *bottom view* of the molecular surface of micelle-bound aS (average structure; Fig. 4, *C–E*) *color-coded* by electrostatic potential as depicted. The predominantly unstructured tail of aS is shown to contrast its highly acidic nature with the repeat region of aS. Electrostatic potential was calculated with APBS (70).

tances between Val-$\gamma^{1,2}$, Leu-$\delta^{1,2}$, and Ile-δ^1 methyl groups across the helices using an isotope labeling procedure where these methyl groups were protonated, with the remainder of the protein deuterated (23). Although none could be detected (data not shown), the nonspecific nature of hydrophobic contacts and distance variation between the helices would make such contacts particularly difficult to detect. In addition, the rotameric states of most side chains were found to be averaged (data not shown).

The aS Tail Region Exhibits Non-uniform Properties—Despite the highly mobile nature of the tail region of aS (Fig. 5, *A* and *B*), residual dipolar couplings (RDCs) of quite large values were obtained for this region. Denatured or unfolded proteins generally exhibit non-zero RDCs (54), which can be attributed to the differential steric obstruction in anisotropic media of the many conformers that contribute to the random coil behavior (55). In the case of aS, an interesting distribution of the RDCs of the highly mobile tail region was observed. Up to Pro[120], RDCs of considerable magnitude were seen, whereas for the remaining tail substantially smaller RDCs were found (Fig. 8*A*). The larger RDCs for the first compared with the second region suggest a difference in shape of the conformational ensembles of these two segments of the tail (55). The positive sign of the N-H RDC values in the C-terminal tail (Fig. 8*A*) reflects that the most ordered conformers of the random coil ensemble have their backbone ordered in a direction parallel to the magnetic field, *i.e.* parallel to the direction in which the gel matrix has been stretched. Finally, small chemical shift changes were induced in the tail by the presence of SDS (Figs. 2*B* and 8*B*), which decrease toward the C terminus, suggesting that the changes do not merely arise from the presence of SDS micelles themselves, but also from the structuring of the repeat region.

DISCUSSION

The structure of micelle-bound aS consists of two curved α-helices, termed helix-N (Val[3]-Val[37]) and helix-C (Lys[45]-Thr[92]), connected by a well ordered, extended linker in an unexpected anti-parallel arrangement, followed by another short extended region (Gly[93]-Lys[97]) and a predominantly unstructured tail (Asp[98]-Ala[140]). The chemical makeup of the applied micelle system (SDS) was found to have little effect on aS structure, as judged by the similarity of aS chemical shifts
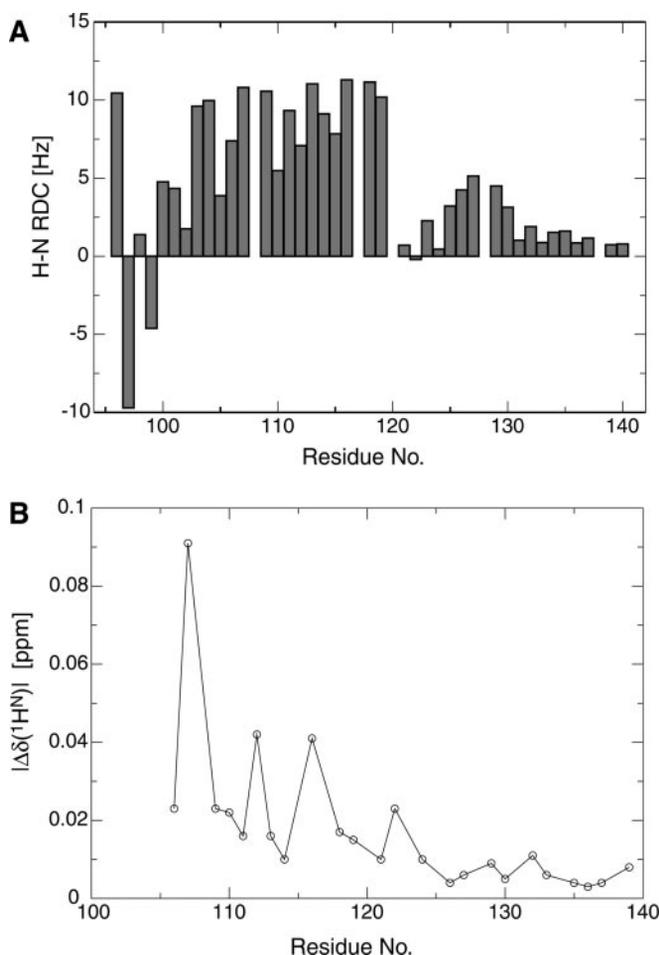
FIG. 8. **Some NMR properties of the aS tail.** *A*, aS N-H residual dipolar couplings measured in a negatively charged stretched polyacrylamide gel (sample D). *B*, H^N chemical shift differences of the tail resonances between SDS:aS molar ratios of 0:1 and 422:1 as a function of residue number.

in the presence SDS-only micelles and mixed micelles composed of DPC and SDS (70:30 molar ratio). The physiological aS target, presynaptic vesicles, exhibit diameters on the order of 50 nm (56), which is about ten times larger than that of an unperturbed SDS micelle. Consequently, the structural implications arising from the less curved and larger surface available to aS in the vesicle-bound state have to be evaluated. An altered helix curvature in the vesicle, compared with the micelle-bound state, will have little effect on the number of residues per turn and helix twist (44). In other words, the local structure encoded by the aS amino acid sequence, which places side chains involved in favorable interactions with the vesicle surface on one side of the helix, remains the same. This is also verified experimentally; for Thr[59]-Ala[90] the side chains lining the inner side of helix-C also face the surface of negatively charged SUV of 300–400 Å diameter (19). Thus, the local structure of helices N and C closely resembles that of the vesicle-bound state. The well ordered, mostly extended helix-helix connector (Leu[38]-Thr[44]) is an interesting feature of the micelle-bound structure. Although the presence of a helix break in the micelle-bound state has been suggested to be a consequence of the small size of the micelle (19), the well ordered helix-helix connector detected here indicates a defined interaction with lipidic surfaces and, hence, corresponds to a stable, low energy conformation. Intriguingly, it is conceivable that Leu[38]-Thr[44] could switch between the conformation we observe in the micelle environment and the previously proposed unin-

terrupted helix when bound to SUV (19) in an environment-dependent manner. Actual presynaptic vesicles are in a complex arrangement with various proteins (57) and, hence, comprise varying environments, which are subject to change during vesicle fusion. An interconversion of the seven Leu[38]-Thr[44] residues between the two conformations would leave helices N and C essentially unperturbed. The short extended stretch following helix-C (Gly[93]-Lys[97]) overlaps with the chaperone-mediated autophagy recognition motif of aS (Val[95]-Gln[99]), which may implicate impaired aS degradation in the pathogenesis of Parkinson's disease (58). Lastly, the aS tail presents itself mainly unstructured, but small shift changes are induced in the tail by the structuring of the repeat region. This observation is complementary to a recent study of aS-polyamine complexes, which concluded that the tail acts as a regulator of aS aggregation (7). In this study polyamines were found to bind Gln[109]-Ala[140], but induce chemical shift changes also in Thr[22]-Gly[93].

The binding of aS to vesicles not only leads to a structuring of aS, but may also impact the stability and membrane fluidity of the vesicle itself. Local differences in structure and dynamics along the helices are therefore of potential importance to aS function. Fast timescale dynamics (sub-nanosecond), which describe fluctuation of individual bond vectors, identify three regions of reduced backbone order, Ala[30]-Val[37], Asn[65]-Val[70], and Glu[83]-Ala[89]. Common to all three regions are two Gly residues in close sequential proximity (Fig. 1). Only repeat IV maintains relatively low sub-nanosecond dynamics despite its two proximate glycines. For helices of globular proteins, the 14.7% Gly content of the aS helices would be exceptionally high, but also for integral membrane proteins it is quite high (59). This suggests that the aS glycines serve a functional role. By conferring elevated dynamics within the aS helix, Gly residues may serve to mitigate a possible reduction in membrane fluidity of aS-coated vesicles. In studies of model membranes the segmental motion of spin-labeled lipids was found to be hindered by the presence of aS (60), and a thermodynamic study of aS-SUV interactions indicated lipid ordering upon aS binding (61). In whole cell membrane preparations of neurons, aS-dependent changes in membrane fluidity were observed (62), whereas for isolated synaptosomal membranes no change in membrane fluidity was detected (63). As a common theme of the numerous biophysical studies on aS, including the present one, an impact of aS on vesicle membrane fluidity and stability is increasingly evident. Consequently, the structure-function relationship points toward a modulation of the fusion propensity of presynaptic vesicles by the presence of aS.

The curved helices N and C exhibit average circle diameters of 153 and 82 Å, respectively, which are considerably larger than the expected diameter of a globular SDS micelle of 46 Å. This can be taken as strong evidence for interactions of the positively charged Lys side chains emanating sideward from the helices with the negatively charged headgroups of SDS, leading to a deformation of the globular micelle along the helix axes to a prolate, ellipsoid particle. This mode of interaction has been proposed for apolipoproteins (64) and seems effective in specifying interactions with negatively charged lipidic surfaces and the targeting of specific membranes. At this point it is also noted that a certain degree of curvature is preferred by the aS helix (10), which has been related to the thermodynamics of the aS-vesicle interaction (61). The two helices exhibit variability in interhelical distances and, in particular the end and beginning of helices N and C, respectively, experience unusually large dynamics on the microsecond timescale, which report on the motions of entire stretches of helix, suggesting that interactions with presynaptic vesicle surfaces will be "fluid."

So far the discussion has focused on aspects of membrane binding relevant to aS function. Are any features of aS membrane binding relevant to understanding aS misfolding? Lipid environments that induce α-helical conformation have been documented to promote aS aggregation into dimers and multimers (14, 21, 22). Here identified features may therefore be relevant for the initiation of aS misfolding. The region Ala[30]-Val[37] is of prime interest, especially given that the A30P substitution, which causes familial Parkinson's disease (65), localizes in this region. It experiences large amplitude dynamics on all timescales, it exhibits reduced helical content and, excepting its two Gly residues, it is identical in sequence to the well behaved Ala[56]-Val[63] region (Fig. 1). Glu[57] and Gln[62] correspond to Gly[31] and Gly[36], and inspection of the structure shows that their side chains do not contact the micelle surface. Taken together, the reduced stability of helical conformation in this region may promote the initial aggregation of aS in non-helical conformation (20).

REFERENCES

1. Goedert, M. (2001) *Nat. Rev. Neurosci.* **2,** 492–501
2. Dev, K. K., Hofele, K., Barbieri, S., Buchman, V. L., and van der Putten, H. (2003) *Neuropharmacology* **45,** 14–44
3. Nussbaum, R. L., and Ellis, C. E. (2003) *N. Engl. J. Med.* **348,** 1356–1364
4. Spillantini, M. G., Schmidt, M. L., Lee, V. M. Y., Trojanowski, J. Q., Jakes, R., and Goedert, M. (1997) *Nature* **388,** 839–840
5. Mezey, E., Dehejia, A. M., Harta, G., Suchy, S. F., Nussbaum, R. L., Brownstein, M. J., and Polymeropoulos, M. H. (1998) *Mol. Psychiatry* **3,** 493–499
6. Conway, K. A., Lee, S. J., Rochet, J. C., Ding, T. T., Williamson, R. E., and Lansbury, P. T. (2000) *Proc. Natl. Acad. Sci. U. S. A.* **97,** 571–576
7. Fernandez, C. O., Hoyer, W., Zweckstetter, M., Jares-Erijman, E. A., Subramaniam, V., Griesinger, C., and Jovin, T. M. (2004) *EMBO J.* **23,** 2039–2046
8. Kahle, P. J., Haass, C., Kretzschmar, H. A., and Neumann, M. (2002) *J. Neurochem.* **82,** 449–457
9. Vekrellis, K., Rideout, H. J., and Stefanis, L. (2004) *Mol. Neurobiol.* **30,** 1–21
10. Davidson, W. S., Jonas, A., Clayton, D. F., and George, J. M. (1998) *J. Biol. Chem.* **273,** 9443–9449
11. George, J. M., Jin, H., Woods, W. S., and Clayton, D. F. (1995) *Neuron* **15,** 361–372
12. Chandra, S., Chen, X. C., Rizo, J., Jahn, R., and Sudhof, T. C. (2003) *J. Biol. Chem.* **278,** 15313–15318
13. Eliezer, D., Kutluay, E., Bussell, R., and Browne, G. (2001) *J. Mol. Biol.* **307,** 1061–1073
14. Narayanan, V., and Scarlata, S. (2001) *Biochemistry* **40,** 9927–9934
15. Jensen, P. H., Nielsen, M. S., Jakes, R., Dotti, G., and Goedert, M. (1998) *J. Biol. Chem.* **273,** 26292–26294
16. Iwai, A., Masliah, E., Yoshimoto, M., Ge, N. F., Flanagan, L., Desilva, H. A. R., Kittel, A., and Saitoh, T. (1995) *Neuron* **14,** 467–475
17. Weinreb, P. H., Zhen, W. G., Poon, A. W., Conway, K. A., and Lansbury, P. T. (1996) *Biochemistry* **35,** 13709–13715
18. Bussell, R., and Eliezer, D. (2003) *J. Mol. Biol.* **329,** 763–778
19. Jao, C. C., Der-Sarkissian, A., Chen, J., and Langen, R. (2004) *Proc. Natl. Acad. Sci. U. S. A.* **101,** 8331–8336
20. Der-Sarkissian, A., Jao, C. C., Chen, J., and Langen, R. (2003) *J. Biol. Chem.* **278,** 37530–37535
21. Cole, N. B., Murphy, D. D., Grider, T., Rueter, S., Brasaemle, D., and Nussbaum, R. L. (2002) *J. Biol. Chem.* **277,** 6344–6352
22. Lee, H. J., Choi, C., and Lee, S. J. (2002) *J. Biol. Chem.* **277,** 671–678
23. Goto, N. K., Gardner, K. H., Mueller, G. A., Willis, R. C., and Kay, L. E. (1999) *J. Biomol. NMR* **13,** 369–374
24. Ulmer, T. S., Ramirez, B. E., Delaglio, F., and Bax, A. (2003) *J. Am. Chem. Soc.* **125,** 9179–9191
25. Chou, J. J., Gaemers, S., Howder, B., Louis, J. M., and Bax, A. (2001) *J. Biomol. NMR* **21,** 377–382
26. Delaglio, F., Grzesiek, S., Vuister, G. W., Zhu, G., Pfeifer, J., and Bax, A. (1995) *J. Biomol. NMR* **6,** 277–293
27. Pervushin, K., Riek, R., Wider, G., and Wuthrich, K. (1997) *Proc. Natl. Acad. Sci. U. S. A.* **94,** 12366–12371
28. Weigelt, J. (1998) *J. Am. Chem. Soc.* **120,** 10778–10779
29. Grzesiek, S., Anglister, J., and Bax, A. (1993) *J. Magn. Reson. Ser. B* **101,** 114–119
30. Hu, J. S., and Bax, A. (1997) *J. Biomol. NMR* **9,** 323–328
31. Hu, J. S., Grzesiek, S., and Bax, A. (1997) *J. Am. Chem. Soc.* **119,** 1803–1804
32. Jaroniec, C. P., Ulmer, T. S., and Bax, A. (2004) *J. Biomol. NMR* **30,** 181–194
33. Chou, J. J., Delaglio, F., and Bax, A. (2000) *J. Biomol. NMR* **18,** 101–105
34. Zhu, G., Xia, Y. L., Nicholson, L. K., and Sze, K. H. (2000) *J. Magn. Reson.* **143,** 423–426
35. Farrow, N. A., Muhandiram, R., Singer, A. U., Pascal, S. M., Kay, C. M., Gish, G., Shoelson, S. E., Pawson, T., Formankay, J. D., and Kay, L. E. (1994) *Biochemistry* **33,** 5984–6003
36. Donaldson, L. W., Skrynnikov, N. R., Choy, W. Y., Muhandiram, D. R., Sarkar, B., Forman-Kay, J. D., and Kay, L. E. (2001) *J. Am. Chem. Soc.* **123,** 9843–9847
37. Delaglio, F., Kontaxis, G., and Bax, A. (2000) *J. Am. Chem. Soc.* **122,** 2142–2143
38. Schwieters, C. D., Kuszewski, J. J., Tjandra, N., and Clore, G. M. (2003) *J. Magn. Reson.* **160,** 65–73
39. Iwahara, J., Schwieters, C. D., and Clore, G. M. (2004) *J. Am. Chem. Soc.* **126,** 5879–5896
40. Grishaev, A., and Bax, A. (2004) *J. Am. Chem. Soc.* **126,** 7281–7292
41. Kuszewski, J. J., and Clore, G. M. (2000) *J. Magn. Reson.* **146,** 249–254
42. Tycko, R., Blanco, F. J., and Ishii, Y. (2000) *J. Am. Chem. Soc.* **122,** 9340–9341
43. Bertini, I., Luchinat, C., and Piccioli, M. (2001) *Methods Enzymol.* **339,** 314–340
44. Kumar, S., and Bansal, M. (1998) *Biophys. J.* **75,** 1935–1944
45. Bansal, M., Kumar, S., and Velavan, R. (2000) *J. Biomol. Struct. Dyn.* **17,** 811–819
46. Lipari, G., and Szabo, A. (1982) *J. Am. Chem. Soc.* **104,** 4546–4559
47. Meiler, J., Prompers, J. J., Peti, W., Griesinger, C., and Bruschweiler, R. (2001) *J. Am. Chem. Soc.* **123,** 6098–6107
48. Tolman, J. R., Al-Hashimi, H. M., Kay, L. E., and Prestegard, J. H. (2001) *J. Am. Chem. Soc.* **123,** 1416–1424
49. Oldfield, E. (2002) *Annu. Rev. Phys. Chem.* **53,** 349–378
50. Case, D. A. (1998) *Curr. Opin. Struc. Biol.* **8,** 624–630
51. Rehage, H., and Hoffmann, H. (1991) *Mol. Phys.* **74,** 933–973
52. Bruce, C. D., Berkowitz, M. L., Perera, L., and Forbes, M. D. E. (2002) *J. Phys. Chem. B* **106,** 3788–3793
53. Garg, G., Aswal, V. K., Kulshreshtha, S. K., and Hassan, P. A. (2004) *Pramana J. Phys.* **63,** 351–355
54. Shortle, D., and Ackerman, M. S. (2001) *Science* **293,** 487–489
55. Louhivuori, M., Fredriksson, K., Paakkonen, K., Permi, P., and Annila, A. (2004) *J. Biomol. NMR* **29,** 517–524
56. Zhang, B., Koh, Y. H., Beckstead, R. B., Budnik, V., Ganetzky, B., and Bellen, H. J. (1998) *Neuron* **21,** 1465–1475
57. Phillips, G. R., Huang, J. K., Wang, Y., Tanaka, H., Shapiro, L., Zhang, W. D., Shan, W. S., Arndt, K., Frank, M., Gordon, R. E., Gawinowicz, M. A., Zhao, Y. M., and Colman, D. R. (2001) *Neuron* **32,** 63–77
58. Cuervo, A. M., Stefanis, L., Fredenburg, R., Lansbury, P. T., and Sulzer, D. (2004) *Science* **305,** 1292–1295
59. Curran, A. R., and Engelman, D. M. (2003) *Curr. Opin. Struct. Biol.* **13,** 412–417
60. Ramakrishnan, M., Jensen, P. H., and Marsh, D. (2003) *Biochemistry* **42,** 12919–12926
61. Nuscher, B., Kamp, F., Mehnert, T., Odoy, S., Haass, C., Kahle, P. J., and Beyer, K. (2004) *J. Biol. Chem.* **279,** 21966–21975
62. Sharon, R., Bar-Joseph, I., Mirick, G. E., Serhan, C. N., and Selkoe, D. J. (2003) *J. Biol. Chem.* **278,** 49874–49881
63. Jo, E., Darabie, A. A., Han, K., Tandon, A., Fraser, P. E., and McLaurin, J. (2004) *Eur. J. Biochem.* **271,** 3180–3189
64. Segrest, J. P., Deloof, H., Dohlman, J. G., Brouillette, C. G., and Anantharamaiah, G. M. (1990) *Proteins* **8,** 103–117
65. Kruger, R., Kuhn, W., Muller, T., Woitalla, D., Graeber, M., Kosel, S., Przuntek, H., Epplen, J. T., Schols, L., and Riess, O. (1998) *Nat. Genet.* **18,** 106–108
66. Anderson, C. A. F., Palmer, A. G., Brunak, S., and Rost, B. (2002) *Structure* **10,** 175–184
67. Dosset, P., Hus, J. C., Blackledge, M., and Marion, D. (2000) *J. Biomol. NMR* **16,** 23–28
68. Sklenar, V. (1995) *J. Magn. Reson. Ser. A* **114,** 132–135
69. Spera, S., and Bax, A. (1991) *J. Am. Chem. Soc.* **113,** 5490–5492
70. Baker, N. A., Sept, D., Joseph, S., Holst, M. J., and McCammon, J. A. (2001) *P. Natl. Acad. Sci. U. S. A.* **98,** 10037–10041